

Dual Virtual Element Methods for Discrete Fracture Matrix Models

Alessio Fumagalli, Eirik Keilegavlen

Department of Mathematics, University of Bergen, Bergen, Norway

alessio.fumagalli@uib.no eirik.keilegavlen@uib.no

November 7, 2017

Abstract

The accurate description of fluid flow and transport in fractured porous media is of paramount importance to capture the macroscopic behaviour of an oil reservoir, a geothermal system, or a CO₂ sequestration site, to name few applications. The construction of accurate simulation model for flow in fractures is challenging due to the high ratios between a fracture's length and width, which makes modeling by lower-dimensional manifolds a natural option. In this paper we present a mixed-dimensional Darcy problem able to describe pressure and Darcy velocity in all the dimensions, *i.e.* in the rock matrix, in the fractures, and in their intersections. Moreover, we present a mixed-dimensional transport problem which, given the Darcy velocity, describes coupled advection and diffusion of a passive scalar into the fractured porous media. The approach can handle both conducting and blocking fractures. Our computational grids are created by coarsening of simplex tessellations that conform to the fractures surfaces. An accurate choice of the discrete approximation of the previous model, by virtual finite element and finite volume, allows us to simulate complex problem with a good balance in term of accuracy and computational cost. We illustrate the performance of our method by comparing to benchmark studies for two-dimensional fractured porous media, as well as a complex three-dimensional fracture geometry.

1 Introduction

Fractures and faults can strongly influence fluid flow in a porous media acting, depending on their permeability and porosity, as a preferential path or a barrier. Due to fracture aperture being several orders of magnitude smaller than any other characteristic sizes in the domain, fracture modeling is one of the main challenges in subsurface problems.

Geological movements, chemical reaction, or infilling processes may substantially alter the local orientation and composition of the material present in the fractures, leading to anisotropies and strong heterogeneities in both fractures and their intersections. It is thus crucial to be able to include also these phenomenological aspects in the conceptual model.

Applications where fractures can be determinant for reservoir behaviour include exploitation of geothermal system, CO₂ storage and sequestration, enhance oil recovery, and nuclear waste disposal. In these fields the solution may dramatically depends on the presence of fractures, thus a correct derivation of suitable mathematical models and their accurate numerical solution is essential.

Small scale fractures can be incorporated in the matrix permeability by analytical or numerical upscaling techniques (*e.g.* see [40, 41, 42] and [36, 27, 34]), thus only macroscopic fractures and faults are considered and explicitly described. However, their number may still be too high for a fully three dimensional representation. Following the idea presented, among the others, in [1, 39, 2, 47, 37, 21, 44, 14] fractures and faults are represented as lower dimensional objects embedded in the rock matrix. For this approximation common terminologies are reduced models, hybrid-dimensional models, and mixed-dimensional models. Fracture aperture becomes thus a coefficient in the equations and not a geometrical constrain for grid

generation. The flow equations are averaged along the normal direction of the fractures obtaining a new set of reduced models suited for the co-dimensional, that is, lower-dimensional, description of fluid flow. Suitable coupling conditions are thus necessary to exchange information between all the objects (rock matrix, fractures, and their intersections).

The reduction of dimensionality is an essential step to overcome most of the difficulties associated to the problem. However, in presence of several fractures which create a complex network more advanced numerical techniques are crucial to obtain an accurate solution in a reasonable amount of time. The main aspect is the geometrical treatment of the fracture grid with respect to the rock matrix grid. The common approaches consider conforming and non-conforming coupling in the case of matching grids or completely a non-matching strategy, in the latter the rock grid is normally considered as a background and the fracture grid may adapt to it up to a certain degree.

In the class of conforming methods, where fracture grids are composed by faces of the rock matrix grid, several numerical schemes have been considered, ranging from finite element [3, 35, 39, 4, 18] to finite volumes [16, 15, 34], mimetic finite difference (MFD) [5, 45], and the newly introduced virtual finite elements (VEM) [10, 26]. All these methods highlight specific advantages for example related to local mass conservation, capability to be implemented in standard software packages, or relax some constraints on grid cell shapes to name a few.

In the class of non-conforming discretization the main tool is a mortar coupling between the rock matrix grid and the fracture grids. The rock mesh is constrained with the position of the fractures but not strictly with the actual fracture meshes, and vice-versa. Some examples are reported in [24, 9, 14] where different type of mortar variables as well as numerical schemes are considered.

Finally, a fully non matching coupling among the grids requires ad-hoc solutions to establish a communication between the fractures and the rock matrix. One possibility is the class of extended finite element methods (XFEM) [19, 30, 28, 12, 44, 20], where a local enrichment with new basis functions is considered to handle the non-conformity, or the class of embedded discrete fracture matrix methods (EDFM) [38, 27, 31, 46], where approximate formulae for fracture-matrix transmissibilities are computed based on geometrical considerations.

In this paper we consider a conforming discretization with the dual virtual element approximation to simulate a mixed-dimensional Darcy problem and a finite volume discretization for the mixed-dimensional transport problem. The first choice is motivated by the flexibility of the virtual element methods with respect to the shape of the grid cells. With this choice it is possible to relax most of the difficulties related with conforming discretization, *e.g.* the computational cost associated to resolve, by the rock matrix grid, a complex system of composed by several intersecting fractures. Moreover, this approximation ensures local mass conservation and is able to consider heterogeneous and anisotropic permeability tensors. The Darcy velocity is thus suited to be used in the mixed-dimensional transport problem. In this case we consider an upwind scheme, extended to handle the mixed-dimensional nature of the problem.

The paper is structured as follows: in Section 2 we present both the physical equations and the reduced model, with the interface conditions that couple the matrix-fracture system and the fracture-fracture system for both the Darcy and transport problems. Section 3 deals with the weak and integral formulation of the previous physical processes. In Section 4 we present the numerical discretization of the problem with an highlight on the enrichment of the finite element spaces. In Section 5 we present some numerical experiments to assess the effectiveness of the proposed method. Finally Section 6 is devoted to conclusions and to ongoing works.

2 Mathematical model

In this section we introduce the mathematical models in the mixed-dimensional setting, *i.e.* the equations couple different spatial dimensions and are able to globally describe the quantities of interest. We present two mathematical models useful for subsurface simulations: the mixed-dimensional Darcy problem, presented in Subsection 2.1, to describe the flow and pressure and the mixed-dimensional transport problem, presented in Subsection 2.2, to describe the motion of a passive scalar transported by the Darcy velocity.

The idea behind the mixed-dimensional formulation is that the fracture aperture is orders of magnitude smaller than other characteristic sizes of the problem. Hence, a straightforward

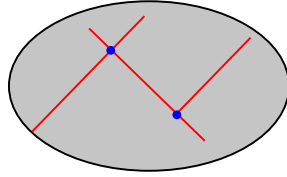


Figure 1: Domain subdivision for $N = 2$. In grey Ω^2 , in red Ω^1 , and in blue Ω^0 .

mesh construction with the two fracture surfaces as constraints would produce high numbers of cells and or low-quality cells due to high aspect ratios or sharp angles. To avoid this geometrical constraint, fractures are represented as lower dimensional objects embedded in the rock matrix. Fracture intersections, and their intersections again, are considered as objects of even lower dimensions. To be specific, in a three-dimensional domain, we consider fracture surfaces as 2d objects, the intersection between two fractures form a 1d line, and two intersection lines can meet in a 0d point. The physical processes are described via reduced models with suitable coupling conditions among the objects of different dimensions. The fracture aperture is now part of the equations and not any more a geometrical constraint. For more details on the derivation of the reduced model we refer to [1, 39, 2, 19, 23, 28, 30, 11, 10, 21, 9, 26, 14].

In the reduced model is a common choice to consider the reduced scalar variables as averaged and the vector variables as integrated along cross section of the fracture. In this work we follow this approach.

In the sequel we indicate by $(\cdot, \cdot)_A$ the scalar product in $L^2(A)$. Moreover, the trace operator on a domain A will be indicated by $\cdot|_A$.

2.1 Mixed-dimensional Darcy problem

Let us consider a regular domain $\Omega \subset \mathbb{R}^N$, for $N > 0$, with outer boundary $\partial\Omega$. The domain Ω is composed by a single, possibly non-connected, equi-dimensional domain Ω^N and several lower-dimensional domains Ω^d for $d < N$, possibly non-connected. Clearly $\cup_{d=0, \dots, N} \Omega^d = \Omega$ and $\Omega^d \cap \Omega^{d'} = \emptyset$ for $d \neq d'$. However, we indicate with $\Gamma^d = \partial\Omega^d \cap \Omega^{d-1}$, which is geometrically equivalent to Ω^{d-1} but it will be more convenient to keep them separate. We have $\Gamma = \cup_{d=0, \dots, N} \Gamma^d$. See Figure 1 as an example of the subdivision.

We are interested to the mixed-dimensional Darcy problem which describes the pressure and velocity fields in Ω . Following the idea presented in [14], we define the pressure compound $p = (p^0, \dots, p^N)$ which represents the pressure in each dimension, indicated as superscript. Similarly we introduce the velocity compound $\mathbf{u} = (0, \mathbf{u}^1, \dots, \mathbf{u}^N, 0)$, which is the velocity field defined in Ω^N or in the tangential spaces of each dimension $d < N$. The meaning of the two 0s will be clarified. In the following problem, each dimension is coupled with the lower dimension; we consider thus two normals \mathbf{n} associated to a $d < N$ -dimensional manifold with respect to its “two sides”, indicated by \mathbf{n}_+ and \mathbf{n}_- . Given a side, by convention the normal points from the higher dimensional to the lower dimensional domain. Moreover, we indicate by the same subscript \cdot_{\pm} the restriction of elements in Ω^d defined on each side of Γ^d through a suitable trace operator.

We consider the Darcy problem for the pressure and velocity as

$$\begin{aligned} \mathbf{u} + K\nabla p &= \mathbf{0} \\ \nabla \cdot \tilde{\mathbf{u}} - [\hat{\mathbf{u}} \cdot \hat{\mathbf{n}}] &= \tilde{f} \quad \text{in } \Omega. \end{aligned} \tag{1a}$$

The $\hat{\cdot}$ notation means “on the higher dimensional object” and the $\tilde{\cdot}$ means “on the lower dimensional object”, *i.e.* fix a dimension d the second of (1a) becomes

$$\nabla \cdot \mathbf{u}^d - \left[\mathbf{u}^{d+1} \cdot \mathbf{n}^{d+1} \right] = f^d \quad 0 \leq d \leq N.$$

In the system (1a) the first equation is defined on the same dimensional domain while the second on mixed-dimensional domain. In the previous equation the differential operators are defined accordingly, *i.e.* for the lower dimensional objects tangential gradient and divergence. In the special 0d case these objects are the null operator. K represents the effective (*i.e.* is already scaled by the “aperture” of each dimension) permeability compound

$K = (1, K^1, \dots, K^N)$, which is a collection of symmetric and positive defined tensors. For $d < N$, K^d is interpreted as laying in the tangent plane of the relevant physical object. The source or sink term f is defined as the compound $f = (f^0, \dots, f^N)$, which are scalar functions defined in each dimension. Finally, the jump operator $[[\hat{\mathbf{u}} \cdot \hat{\mathbf{n}}]] = \sum_{\pm} \hat{\mathbf{u}} \cdot \hat{\mathbf{n}}|_{\pm}$ is done on each side of Ω^{d-1} viewed as immersed in Ω^d .

The first equation in (1a) is the generalized Darcy law in each dimension, note that for the 0d case it is simply an identity. The second equation of (1a) represents the conservation of mass. The divergence term describes the conservation of the mass in the dimension and the flow exchange with the lower dimensional domain (see the derivation of the weak formulation in Section 3), while the second represents the inflow/outflow from the higher dimension. Due to the definition of the velocity compound, for $d = N$ equation (1a) the inflow/outflow from the “higher dimension” is null. While for $d = 0$ the second equation represents the continuity of the fluxes for the 1-dimensional objects involved in the intersection.

It is important to note that the mixed-dimensional problem requires that the quantities defined on Ω^{d-1} are in communication with the quantities defined on Ω^d and not directly with quantities defined on Ω^{d+1} .

The coupling conditions between two subsequent dimensions are defined for the each side as

$$\hat{\mathbf{u}} \cdot \hat{\mathbf{n}}|_{\pm} + k_* (\check{p} - \hat{p}|_{\pm}) = 0 \quad \text{on } \Gamma. \quad (1b)$$

The k_* is the effective normal permeability, defined as $k_* = (k_*^0, \dots, k_*^{N-1})$. Clearly, equation (1b) is valid between dimension d and $d + 1$ for $0 \leq d < N$. Note that in equation (1b) it is possible to define different effective normal permeability on each side \pm , however, to ease the notation, we assume only one single value.

Boundary conditions need to be assigned to obtain a well-posed problem. We indicate by $\partial\Omega_{out}^d$ the (possibly empty) portion of the boundary of Ω^d that intersect the boundary of Ω , for $d > 0$. We introduce also $\partial\Omega_{in}^d$ the portion of boundary of Ω^d that do not intersect the boundary of Ω , for $d > 0$. For simplicity we assume only pressure boundary conditions on $\partial\Omega_{out}^d$, given as

$$p^d = \bar{p}^d \quad \text{on } \partial\Omega_{out}^d, \quad (1c)$$

with \bar{p}^d is a given pressure at the boundary for each $d > 0$. On the internal portion $\partial\Omega_{in}^d$, for $d > 0$, we assign the so-called “tip-condition”, namely

$$\mathbf{u}^d \cdot \mathbf{n}|_{\partial\Omega_{in}^d} = 0 \quad \text{on } \partial\Omega_{in}^d, \quad (1d)$$

where in the previous equation \mathbf{n} stands for the outward unit normal of $\partial\Omega_{in}^d$.

Equation (1) is the mixed-dimensional Darcy problem, formulated in terms of pressure and velocity. The problem (1) may be recast into a pure pressure formulation, however the numerical scheme introduced in Section 4 considers explicitly the pressure and velocity fields as unknowns.

Following the idea presented in [24, 14, 13], it is possible to write problem (1) in a more compact form similar to the standard Darcy formulation. To this end, we introduce the following divergence operator between dimensions as $\mathfrak{D} : \Omega \times \Gamma \rightarrow \Omega$ such that

$$\mathfrak{D} \cdot \mathbf{w} = \nabla \cdot \check{\mathbf{w}} - [[\hat{\mathbf{q}} \cdot \hat{\mathbf{n}}]],$$

as well as a mixed-dimensional gradient operator $\mathfrak{D} : \Omega \rightarrow \Omega \times \Gamma$ such that

$$\mathfrak{D}q = [\nabla\check{q}, \check{q} - \hat{q}]^T.$$

Considering the Darcy velocity composed by \mathbf{u} in Ω and $\mathbf{u} \cdot \mathbf{n}$ on Γ , system (1) becomes

$$\begin{aligned} \mathbf{u} + \mathfrak{K}\mathfrak{D}p &= 0 & \text{in } \Omega \times \Gamma \\ \mathfrak{D} \cdot \mathbf{u} &= f & \text{in } \Omega \end{aligned} \quad (1a, 1b\text{-bis})$$

In the previous equation \mathfrak{K} is defined accordingly to include both the effective tangential and normal permeabilities.

2.2 Mixed-dimensional transport problem

Once the problem (1) is solved, the velocity field \mathbf{u} can be used to describe the mixed-dimensional transport problem. We consider the same splitting of Ω as in Subsection 2.1. We introduce the concentration compound, following the idea presented in [29], as $c = (0, c^1, \dots, c^N, 0)$, with $0 \leq c \leq 1$ for all d , to describe the portion of a scalar passive in a grid cell. We indicate by t the time variable and $(0, T)$ the time interval.

The model is the following, given \mathbf{u} find c such that

$$\check{\phi}\epsilon\partial_t\check{c} + \nabla \cdot (\check{\mathbf{u}}\check{c}) - \llbracket \hat{\mathbf{u}} \cdot \hat{\mathbf{n}}\check{c} \rrbracket = \check{r} \quad \text{in } \Omega \times (0, T), \quad (2a)$$

where ϵ represents the ‘‘fracture aperture’’ in each dimension, we have $\epsilon = (\epsilon^0, \dots, \epsilon^{N-1}, 1)$. For fracture intersections, the aperture is naturally interpreted as the area of the cross-section (or volume in 0d). We assume that $\epsilon^d > 0$ for all $0 \leq d \leq N$. For simplicity we assume that ϵ does not depend on time. We have indicated with $\partial_t c$ the time derivative of c . Finally, ϕ and r are the porosity and a scalar source/sink term in each dimension, represented as compounds.

In (2a) the divergence term models the conservation of c in the current dimension d and the flow exchange with the lower dimension $d - 1$. The jump operator describes the flow exchange with the higher dimension $d + 1$. The coupling conditions, related to the definition of inflow/outflow of the lower-dimensional objects, associated to (2a) are

$$\hat{c}|_{\pm}(\mathbf{x}) = \begin{cases} \hat{c}|_{\pm}(\mathbf{x}) & \text{if } \hat{\mathbf{u}} \cdot \hat{\mathbf{n}}|_{\pm} \geq 0 \\ \check{c}(\mathbf{x}) & \text{otherwise} \end{cases} \quad \text{on } \Gamma \times (0, T). \quad (2b)$$

Also in this case, problem (2) couples the concentration defined on Ω^d with Ω^{d-1} and Ω^{d+1} , but not directly with Ω^{d-2} or Ω^{d+2} .

With (2a) we need to assign initial condition \bar{c} for the concentration c , as

$$c(t = t_{ini}) = \bar{c} \quad \text{on } \Omega \times \{0\}, \quad (2c)$$

with t_{ini} the initial time. Finally, on the inflow part of the outer boundary we assign a boundary condition \bar{c} for (2a)

$$c = \bar{c} \quad \text{on } \partial\Omega_{out, \mathbf{u} \cdot \mathbf{n} > 0}^d \times (0, T), \quad (2d)$$

where $\partial\Omega_{out, \mathbf{u} \cdot \mathbf{n} > 0}^d$ is the portion of $\partial\Omega_{out}^d$ such that an inflow occurs. Equation (2) is the mixed-dimensional transport problem.

It is possible to write (2) with the formalism introduced at the end of the previous part, obtaining

$$\phi\epsilon\partial_t c + \mathfrak{D} \cdot (\mathbf{u}c) = r \quad \text{in } \Omega \times (0, T), \quad (2a\text{-bis})$$

which is a general form of a conservative equation in the mixed-dimensional setting.

3 Weak and integral formulation

In the view of introducing the numerical approximations, in this part we consider the weak formulation of (1) and the integral formulation of (2).

3.1 Weak formulation of mixed-dimensional Darcy problem

We introduce the functional spaces suitable to approximate the pressure and the velocity. Considering a fixed-dimensional domain Ω^d we have for the pressure $p^d \in Q^d = L^2(\Omega^d)$, for $d > 0$, and $p^0 \in Q^0 = \mathbb{R}$. For the velocity we consider, for $d > 0$, the Hilbert space

$$V^d = \left\{ \mathbf{v} \in H_{div}(\Omega^d) : \mathbf{v} \cdot \mathbf{n}|_{\pm} \in L^2(\Gamma^{d-1}) \right\}$$

The additional condition in V^d is related to the Robin-type nature of the condition (1b), see [39, 26]. The global spaces Q and V are defined as the union of the local spaces.

We introduce now the bilinear forms associated to the problem (1). We have $a^d(\cdot, \cdot) : V^d \times V^d \rightarrow \mathbb{R}$ and $b^d(\cdot, \cdot) : V^d \times Q^d \rightarrow \mathbb{R}$, defined as

$$a^d(\mathbf{w}, \mathbf{v}) = (K^{-1}\mathbf{w}, \mathbf{v})_{\Omega^d} \quad b^d(\mathbf{w}, q) = (\nabla \cdot \mathbf{w}, q)_{\Omega^d},$$

with $\mathbf{w}, \mathbf{v} \in V^d$ and $q \in Q^d$. For the coupling between dimensions, $d > 0$, we introduce $\alpha^d(\cdot, \cdot) : V^d \times V^d \rightarrow \mathbb{R}$ and $\beta^{d,d-1}(\cdot, \cdot) : V^d \times Q^{d-1} \rightarrow \mathbb{R}$ defined as

$$\alpha^d(\mathbf{w}, \mathbf{v}) = \sum_{\pm} (\eta_*^d \mathbf{w} \cdot \mathbf{n}|_{\pm}, \mathbf{v} \cdot \mathbf{n}|_{\pm})_{\Omega^{d-1}}$$

$$\beta^{d,d-1}(\mathbf{w}, q) = \sum_{\pm} (\mathbf{w} \cdot \mathbf{n}|_{\pm}, q)_{\Omega^{d-1}},$$

where $\mathbf{w}, \mathbf{v} \in V^d$ and $q \in Q^{d-1}$. In the previous definition we have η_*^d the inverse of k_*^d and \mathbf{n} the normal of Ω^{d-1} in the tangent space of Ω^d . The global bilinear forms are defined by $a(\cdot, \cdot) : V \times V \rightarrow \mathbb{R}$ and by $b(\cdot, \cdot) : V \times Q \rightarrow \mathbb{R}$ as

$$a(\mathbf{w}, \mathbf{v}) = \sum_{d>0} a^d(\mathbf{w}^d, \mathbf{v}^d) + \alpha^d(\mathbf{w}^d, \mathbf{v}^d)$$

$$b(\mathbf{w}, q) = \sum_{d>0} b^d(\mathbf{w}^d, q^d) + \beta^{d,d-1}(\mathbf{w}^d, q^{d-1}),$$

with $\mathbf{w}, \mathbf{v} \in V$ and $q \in Q$. We can introduce the weak formulation of (1), which reads: find $(\mathbf{u}, p) \in V \times Q$ such that

$$\begin{aligned} a(\mathbf{u}, \mathbf{v}) + b(\mathbf{v}, p) &= G(\mathbf{v}) \quad \forall \mathbf{v} \in V \\ b(\mathbf{u}, q) &= F(q) \quad \forall q \in Q \end{aligned} \quad (3)$$

where the functionals are defined as

$$F(q) = \sum_d (f^d, q^d)_{\Omega^d} \quad G(\mathbf{v}) = - \sum_{d>0} (\mathbf{v} \cdot \mathbf{n}|_{\partial\Omega_{out}^d}, \bar{p}^d)_{\partial\Omega_{out}^d}.$$

3.2 Integral formulation of mixed-dimensional transport problem

In Subsection 4.2 we consider a finite volume approximation of problem (2), thus we introduce here its integral formulation.

Considering a suitable sub-domain of Ω^d called E , later will be a cell of the computational grid, we integrate equation (2) obtaining the following

$$\begin{aligned} &(\check{\phi} \check{\partial}_t \check{c}, 1)_E + (\check{\mathbf{u}} \cdot \check{\mathbf{n}}|_{\partial E}, \check{c}|_{\partial E})_{\partial E} + \\ &\sum_{\pm} (\check{\mathbf{u}} \cdot \check{\mathbf{n}}|_{I, \pm}, \check{c}|_{I, \pm})_{I, \pm} - (\hat{\mathbf{u}} \cdot \hat{\mathbf{n}}|_{E, \pm}, \hat{c}|_{E, \pm})_E = (\check{r}, 1)_E \end{aligned} \quad (4)$$

where $I = E \cap \Omega^{d-1}$ is the intersection between E and the lower dimensional domain Ω^{d-1} , which can be an empty set.

In (4), we notice the term depending on I which describe the inflow/outflow exchange between the current and lower dimensions. Condition (2b) applies also in this case.

4 Numerical discretization

In this section we introduce the numerical scheme used to solve the mixed-dimensional problems (1) and (2). In particular, for the former we consider the lowest order dual virtual element method approximation (VEM), while for the latter we employ a finite volume discretization with an upwind scheme and implicit Euler in time.

Let us introduce a suitable tessellation \mathcal{T} of Ω in polytopes indicated by E , such that

$$\mathcal{T} = \cup_i E_i \quad \text{and} \quad E_i \cap E_j = \emptyset \quad \text{for } i \neq j.$$

We denote by h_E the diameter of E , by \mathbf{x}_E the centre of E , by $\mathcal{E}(E) = \{e \in \partial E\}$ the set of faces for the cell E , and by \mathbf{n}_e with $e \in \mathcal{E}(E)$ the unit normal of e pointing outward with respect to the internal part of E . The term faces indicates proper faces for the 3d grid, edges for the 2d grids, and vertices for the 1d grids. We indicate also by $h = \max_{E \in \mathcal{T}} h_E$ the characteristic grid size and by $\mathcal{E} = \cup_{E \in \mathcal{T}} \mathcal{E}(E)$ the set of the grid faces. It is important to note that the polytopes may have different spatial dimension, *i.e.* they are 3d or 2d or 1d or 0d objects. However, fixing a single dimension d the cells of the grid belongs to Ω^d .

For simplicity, both problems (1) and (2) use the same computational grid.

In Subsection 4.1 we present the discretization for problem (1), while in Subsection 4.2 the numerical approximation for problem (2). Finally, in Subsection 4.3 we introduce a coarsening strategy used in the numerical examples.

4.1 Mixed-dimensional dual VEM discretization

We present a numerical scheme to solve the mixed-dimensional Darcy problem (1) in presence of polytopes in the grid. The resulting scheme will be locally and globally conservative, thus suitable to approximate the velocity field used in (2). We consider the dual virtual element method of lowest order degree, for more details on the derivation and on the analysis see [7, 17, 6, 10, 8, 9, 26].

We introduce finite dimensional spaces to approximate the Darcy velocity \mathbf{u} and the pressure p in each element of the grid. For simplicity we consider a single dimension and, if not essential, we drop the superscript d to simplify notation. Again the differential operators are understood to be defined on the tangential space. Given an element E the local discretization space for the pressure is $Q_h^d(E) = \mathbb{P}_0(E) \subset L^2(E)$, where $\mathbb{P}_r(E)$ is the space of polynomial of order r on the domain E . For the velocity we need to introduce the following space

$$V_h^d(E) = \{\mathbf{v} \in H_{div}(E) : \mathbf{v} \cdot \mathbf{n}_e \in \mathbb{P}_0(e) \forall e \in \mathcal{E}(E), \\ \nabla \cdot \mathbf{v} \in \mathbb{P}_0(E), \nabla \times \mathbf{v} = \mathbf{0}\}.$$

The shape of the functions in $V_h^d(E)$ is not defined a-priori and are implicitly defined by $V_h^d(E)$. The curl-free conditions necessary to uniquely define the elements in $V_h^d(E)$. We indicate by V_h^d the velocity approximation space in the same dimensional grid and by V_h the global discretization space for the velocity formed by the compound (V_h^1, \dots, V_h^N) . Similarly, Q_h^d indicates the pressure approximation space in the same dimension d while Q_h is the global discretization space. For the velocity, we impose to the faces which are not in contact with different dimensions to be single value. Otherwise, the degree of freedom is doubled and connected through the coupling condition (1b) to the lower dimensional object. See Figure 2 for an example.

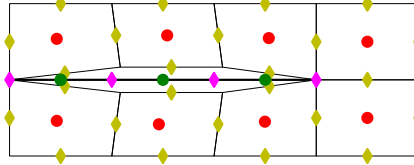


Figure 2: Representation of the degrees of freedom for a 2d and 1d grid. The pressure *dof* are represented by circles, red for the 2d grid and green for the 1d. The velocity *dof* are depicted by yellow diamonds for the 2d grid and purple diamonds for the 1d. The nodes of the 2d grid are moved only for visualization purpose.

With the previous definition of Q_h and V_h it is immediate to approximate the bilinear form b for all the dimensions as well as the bilinear forms associated with the coupling conditions, α^d and $\beta^{d,d-1}$. The functionals F and G are discretized similarly. The bilinear forms a^d are not immediately computable with the degrees of freedom introduced, but require the definition of a suitable projection operator. First we introduce the local space

$$\mathcal{V}_h^d(E) = \left\{ \mathbf{v} \in V_h^d(E) : \mathbf{v} = K \nabla v, \text{ for a } v \in \mathbb{P}_1(E) \right\},$$

and the projection operator is defined as $\Pi_0 : V_h^d(E) \rightarrow \mathcal{V}_h^d(E)$ such that given $\mathbf{v} \in V_h^d(E)$ we have $a^d(\mathbf{v} - \Pi_0 \mathbf{v}, \mathbf{w}) = 0$ for all $\mathbf{w} \in \mathcal{V}_h^d(E)$. Note that the space $\mathbb{P}_1(E)$ in the definition of $\mathcal{V}_h^d(E)$ will be approximated by a (tangential) monomial basis. With this property it is possible to split the bilinear form a^d in a term on $\mathcal{V}_h^d(E)$ and one on the a^d -orthogonal space of $\mathcal{V}_h^d(E)$, namely

$$a^d(\mathbf{u}, \mathbf{v}) = a^d(\Pi_0 \mathbf{u}, \Pi_0 \mathbf{v}) + a^d(T_0 \mathbf{u}, T_0 \mathbf{v})$$

with $T_0 = I - \Pi_0$. The first bilinear form is now fully computable with the velocity degrees of freedom introduced before and represent a consistency term with respect to $a^d(\mathbf{u}, \mathbf{v})$. The second term is not yet computable and can be replaced by a stabilization term. Following the ideas presented in [17, 6, 8], we approximate by

$$a^d(T_0 \mathbf{u}, T_0 \mathbf{v}) \approx \varsigma s^d(\mathbf{u}, \mathbf{v})$$

where $s^d : V_h^d(E) \times V_h^d(E) \rightarrow \mathbb{R}$ is the bilinear form associated with the stabilization and $\varsigma = \varsigma(d) \in \mathbb{R}^+$ is a scaling parameter described in the sequel. In details, denoting by φ an element of the basis for $V_h^d(E)$, in our case we consider

$$s^d(\varphi_\omega, \varphi_\theta) = \sum_{i=1}^{N_{dof}} dof_i(T_0 \varphi_\omega) dof_i(T_0 \varphi_\theta),$$

with N_{dof} the total number of velocity degrees of freedom of the element E . We introduce the discrete version $a_h^d : V_h^d(E) \times V_h^d(E) \rightarrow \mathbb{R}$ of the bilinear form a^d , defined as

$$a_h^d(\mathbf{u}, \mathbf{v}) = a^d(\Pi_0 \mathbf{u}, \Pi_0 \mathbf{v}) + \varsigma s^d(\mathbf{u}, \mathbf{v}),$$

and the discrete version of the weak problem (3), which reads: find $(\mathbf{u}, p) \in V_h \times Q_h$ such that

$$\begin{aligned} a_h(\mathbf{u}, \mathbf{v}) + b(\mathbf{v}, p) &= G(\mathbf{v}) \quad \forall \mathbf{v} \in V_h \\ b(\mathbf{u}, q) &= F(q) \quad \forall q \in Q_h \end{aligned} \quad (5)$$

where $a_h(\mathbf{u}, \mathbf{v}) = \sum_{d>0} a_h^d(\mathbf{u}^d, \mathbf{v}^d) + \alpha^d(\mathbf{u}^d, \mathbf{v}^d)$. How to represent the discrete problem in term of local matrix computations refer to [7, 26].

The stabilization parameter ς is used to impose the scaling on h of the stabilization term equivalent to the consistency term. In practice we require that, for a fixed dimension d , there exists $\iota_*, \iota^* \in \mathbb{R}^+$, independent from the discretization, such that

$$\iota_* a^d(\Pi_0 \mathbf{v}, \Pi_0 \mathbf{v}) \leq \varsigma s^d(\mathbf{v}, \mathbf{v}) \leq \iota^* a^d(\Pi_0 \mathbf{v}, \Pi_0 \mathbf{v}) \quad \forall \mathbf{v} \in V_h^d.$$

Following [26], by a scaling computation it is possible to evaluate the dependency of ς from the local grid size h_E , obtaining the following relation for a fix dimension d

$$\varsigma(E) = h_E^{2-d}.$$

Note that this expression is local and independent from the maximal dimension N of the problem.

We finally introduce the matrix formulation associated with the problem (5). Considering the following matrices

$$\begin{aligned} [A_d]_{ij} &= a_h^d(\varphi_j, \varphi_i) + \alpha^d(\varphi_j, \varphi_i), \\ [B_d]_{ij} &= b^d(\varphi_j, \psi_i), \quad [C_{d,d-1}]_{ij} = \beta^{d,d-1}(\varphi_j, \psi_i) \end{aligned}$$

and vectors

$$[G_d]_i = G(\varphi_i), \quad [F_d]_i = F(\psi_i),$$

where ϕ are basis for the pressure and $[\cdot]_{i,j}$ indicates the element (i, j) in the matrix, a similar notation is used for vectors. The global problem reads for $N = 3$, solve the following linear

system

$$\begin{bmatrix} A_3 & B_3 & 0 & C_{3,2} & 0 & 0 & 0 & 0 \\ B_3^\top & 0 & 0 & 0 & 0 & 0 & 0 & 0 \\ 0 & 0 & A_2 & B_2 & 0 & C_{2,1} & 0 & 0 \\ C_{3,2}^\top & 0 & B_2^\top & 0 & 0 & 0 & 0 & 0 \\ 0 & 0 & 0 & 0 & A_1 & B_1 & 0 & C_{1,0} \\ 0 & 0 & C_{2,1}^\top & 0 & B_1^\top & 0 & 0 & 0 \\ 0 & 0 & 0 & 0 & 0 & 0 & I & 0 \\ 0 & 0 & 0 & 0 & C_{1,0}^\top & 0 & 0 & 0 \end{bmatrix} \begin{bmatrix} \mathbf{u}_3 \\ p_3 \\ \mathbf{u}_2 \\ p_2 \\ \mathbf{u}_1 \\ p_1 \\ \mathbf{u}_0 \\ p_0 \end{bmatrix} = \begin{bmatrix} G_3 \\ F_3 \\ G_2 \\ F_2 \\ G_1 \\ F_1 \\ 0 \\ 0 \end{bmatrix}$$

Where \mathbf{u}_d and p_d represent the vectors associated with the degrees of freedom of velocity and pressure in each dimension d . We notice that the \mathbf{u}_0 is considered only for clearness and to preserve the structure of the matrix. In practice, it is possible to remove \mathbf{u}_0 from the system.

4.2 Mixed-dimensional FV discretization

We consider now the discretization of equation (4). For simplicity, we consider a fixed time step Δt such that $T/\Delta t$ is an integer number. An implicit Euler is consider in time obtaining the semi-discrete version of (4)

$$\frac{(\check{\phi}\check{c}^{n+1} - \check{c}^n, 1)_E}{\Delta t} + (\check{\mathbf{u}} \cdot \check{\mathbf{n}}|_{\partial E}, \check{c}^{n+1}|_{\partial E})_{\partial E} + \sum_{\pm} (\check{\mathbf{u}} \cdot \check{\mathbf{n}}|_{I,\pm}, \check{c}^{n+1}|_{I,\pm})_{I,\pm} - (\hat{\mathbf{u}} \cdot \hat{\mathbf{n}}|_{E,\pm}, \hat{c}^{n+1}|_{E,\pm})_E = (\check{r}^{n+1}, 1)_E,$$

where the superscript indicates the time step index, clearly $c^0 = \bar{c}$. The approximation of the boundary integrals in the previous equation rely on an upwind scheme. We introduce a Kronecker-type delta as

$$\delta_{\mathbf{u} \cdot \mathbf{n}} = \begin{cases} 1 & \text{if } \mathbf{u} \cdot \mathbf{n} \geq 0 \\ 0 & \text{else} \end{cases}.$$

Given a cell face $e \in \mathcal{E}(E)$ we have

$$(\check{\mathbf{u}} \cdot \check{\mathbf{n}}|_e, \check{c}^{n+1}|_e)_e = \check{\mathbf{u}} \cdot \check{\mathbf{n}}|_e [\delta_{\check{\mathbf{u}} \cdot \check{\mathbf{n}}|_e} \check{c}^{n+1}(E) + (1 - \delta_{\check{\mathbf{u}} \cdot \check{\mathbf{n}}|_e}) \check{c}^{n+1}(L)]$$

where the cells K and L share the face e . Given a cell E such that one of its face e intersect one side of I , we get

$$(\hat{\mathbf{u}} \cdot \hat{\mathbf{n}}|_e, \hat{c}^{n+1}|_e)_e = \hat{\mathbf{u}} \cdot \hat{\mathbf{n}}|_e [\delta_{\hat{\mathbf{u}} \cdot \hat{\mathbf{n}}|_e} \hat{c}^{n+1}(E) + (1 - \delta_{\hat{\mathbf{u}} \cdot \hat{\mathbf{n}}|_e}) \hat{c}^{n+1}(\check{e})]$$

where \check{e} indicates a cell in the co-dimensional grid which is in communication with the face e . Finally, on side of the last term of the semi-discrete problem can be approximated by

$$(\hat{\mathbf{u}} \cdot \hat{\mathbf{n}}|_E, \hat{c}^{n+1}|_E)_E = \hat{\mathbf{u}} \cdot \hat{\mathbf{n}}|_E [\delta_{\hat{\mathbf{u}} \cdot \hat{\mathbf{n}}|_E} \hat{c}^{n+1}(\hat{E}) + (1 - \delta_{\hat{\mathbf{u}} \cdot \hat{\mathbf{n}}|_E}) \hat{c}^{n+1}(E)]$$

where \hat{E} represent the cell in the higher dimensional grid which has a face in communication with the cell E . The previous condition applies to both the equi and co-dimensional coupling, see Figure 3 as an example. Note that the chosen discretization is compatible with the coupling condition (2b).

The matrix formulation of the transport problem consider the introduction of the following matrices

$$[M_d]_{ii} = \frac{(\phi^d \epsilon^d, 1)_i}{\Delta t}, \quad [U_d]_{ii} = \sum_{j \in \mathcal{N}(i), e \in \tilde{i} \cap \tilde{j}} (\mathbf{u}^d \cdot \mathbf{n}^d|_e, \delta_{\mathbf{u}^d \cdot \mathbf{n}^d|_e})_e,$$

$$[U_d]_{ij} = \sum_{j \in \mathcal{N}(i), e \in \tilde{i} \cap \tilde{j}} (\mathbf{u}^d \cdot \mathbf{n}^d|_e, 1 - \delta_{\mathbf{u}^d \cdot \mathbf{n}^d|_e})_e$$

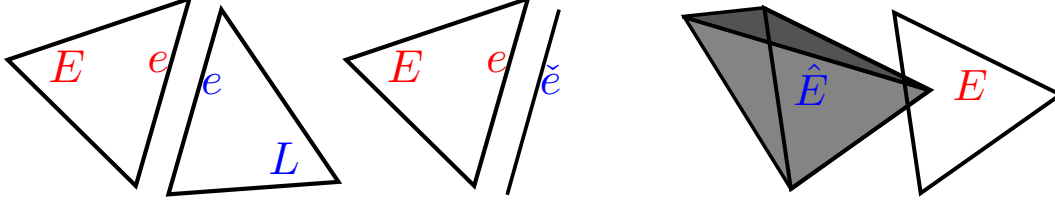


Figure 3: Representation of the coupling between dimension for the upwind discretization scheme. On the left between two cells in the same dimension d , in the centre between a d -dimensional cell and a $d-1$ -dimensional cell, and on the right between a $d+1$ -dimensional cell and a d -dimensional cell.

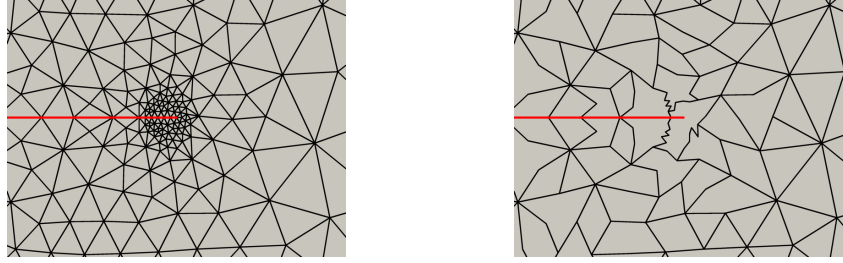


Figure 4: Example of the coarsening strategy adopted. In the left part the computational grid is artificially forced to be more fine at the tip of a fracture, while in the right the resulting grid after the coarsening. Clearly the cell measures are comparable.

where $\mathcal{N}(E)$ is the set of all neighbour cells of E , i and j indicate the generic cell i and j , and e is a face in common with i and j . For the coupling between dimensions we have

$$[U_{d,d-1}]_{ii} = \sum_{j \in \mathcal{N}^{d-1}(i)} (\mathbf{u}^d \cdot \mathbf{n}^d|_j, \delta_{\mathbf{u}^d \cdot \mathbf{n}^d|_j})_j$$

$$[U_{d,d-1}]_{ij} = \sum_{j \in \mathcal{N}^{d-1}(i)} (\mathbf{u}^d \cdot \mathbf{n}^d|_j, 1 - \delta_{\mathbf{u}^d \cdot \mathbf{n}^d|_j})_j,$$

where $\mathcal{N}^{d-1}(E)$ is the set of all neighbour cells of E in the lower dimensional grid. We obtain also

$$[U_{d,d+1}]_{ii} = - \sum_{j \in \mathcal{N}^{d+1}(i)} (\mathbf{u}^{d+1} \cdot \mathbf{n}^{d+1}|_i, \delta_{\mathbf{u}^{d+1} \cdot \mathbf{n}^{d+1}|_i})_i$$

$$[U_{d,d+1}]_{ij} = - \sum_{j \in \mathcal{N}^{d+1}(i)} (\mathbf{u}^{d+1} \cdot \mathbf{n}^{d+1}|_i, 1 - \delta_{\mathbf{u}^{d+1} \cdot \mathbf{n}^{d+1}|_i})_i,$$

where $\mathcal{N}^{d+1}(E)$ is the set of all neighbour cells of E in the higher dimensional grid. We finally obtain the following linear system to be inverted

$$\begin{bmatrix} U_3 + M_3 & U_{3,2} & 0 & 0 \\ U_{2,3} & U_2 + M_2 & U_{2,1} & 0 \\ 0 & U_{1,2} & U_1 + M_1 & U_{1,0} \\ 0 & 0 & U_{0,1} & 0 \end{bmatrix} \begin{bmatrix} c_3^{n+1} \\ c_2^{n+1} \\ c_1^{n+1} \\ c_0^{n+1} \end{bmatrix} = \begin{bmatrix} \zeta_3^{n,n+1} \\ \zeta_2^{n,n+1} \\ \zeta_1^{n,n+1} \\ 0 \end{bmatrix}$$

Where c_d represents the vector associated with the degrees of freedoms of the concentration in each dimension d . In the previous linear system ζ_d represent the right-hand side, combination of the source term r_d^{n+1} and the concentration at the previous time step. We get

$$\zeta_d^{n,n+1} = M_d c_d^n + r_d^{n+1}.$$

4.3 Coarsening strategy

The creation of conforming grids in presence of several fractures can be a challenging task, especially in 3d. In this work we rely on the Gmsh mesh generator [33] for the construction of the computational grids. In presence of almost intersecting fractures or small fracture branches, the grid may result composed by a high number of simplex cells. To overcome this difficulty we exploit one of the advantages of the VEM able to handle cells of arbitrary geometry. To be specific, the theory developed in [7, 17, 6, 8] requires star-shaped cells, however the study carry out in [25] shows that the VEM are able to handle also cells with cuts.

Motivated by these observations we introduce a coarsening scheme that merges small simplex cells into larger polygons or polyhedra. Starting from a given simplex grid, the algorithm computes the measure (area or volume) of the cells. Given the cell c with the smallest measure, it will be merged to one or more neighbouring cells, based on their respective measure, creating a new coarse cell. The clustering stops when a cell measure threshold is reached.

The algorithm does not guarantee any regularity of the final grid, see an example in Figure 4.

5 Applicative examples

We present some examples and test cases to asses the previous models and numerical schemes. The first example, presented in Subsection 5.1, consider an extensive validation of the mixed-dimensional Darcy problem solved by VEM through a benchmark study presented in [22]. The second test case, in Subsection 5.2, consider the transport problem and analyse the impact of the coarsening strategy on the results. Finally, in Subsection 5.3 a realistic 3d example is introduced and studied. In all the forthcoming examples we assume unitary porosity and zero source term for the concentration and Darcy equations. The other parameters will be specified.

In all of the forthcoming examples a “Blue to Red Rainbow” colour map is used.

The examples are part of the PorePy package, which is a simulation tool for fractured and deformable porous media written in Python. See github.com/pmgbergen/porepy for more details.

5.1 Benchmark comparison

To validate the presented model, we consider benchmark 1 and 4 presented in [22]. We carry out the same type of analysis in the same setting, for more detail of problem setting refer to the aforementioned work.

5.1.1 Benchmark 1: Regular Fracture Network

The problem is inspired by [32] with different boundary conditions and material properties. We have unitary permeability matrix and fracture aperture equal to 10^{-4} . We consider two possibility for fracture permeability: high conductive with permeability 10^4 and low conductive with permeability 10^{-4} . In the former case the solution obtained with the method presented previously along with the computational grid are presented in Figure 5 left, the latter in the right. We can notice a good agreement between the computed and the reference solutions, reported in [22]. We point out that some of the elements present in Figure 5 are not convex.

To have a more detailed comparison we consider two plots over line for the permeable case and one for the blocking case, shown in Figure 6. From now on, the method presented in this paper is labelled as VEM. Also in this case we have a good agreement between the computed and reference solutions, comparable to others methods able to represent blocking fractures. Small oscillations are related to mesh effects.

Finally, in both cases we consider the error decay for both the rock matrix and the system of fractures. We consider a family of three meshes where the coarsening is applied in all the cases. We obtain again non-convex elements in all the meshes. Figure 7 plots for conductive

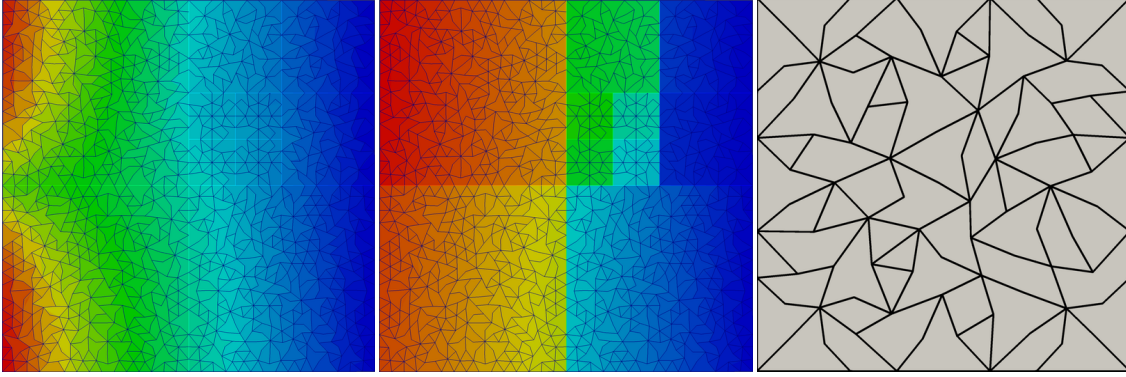


Figure 5: Benchmark 1. On the left: pressure solution (range (1,1.6)) with conductive fractures and computational grid. On the centre: pressure solution (range (1,3.6)) with blocking fractures and computational grid. On the right: zoom of the grid used.

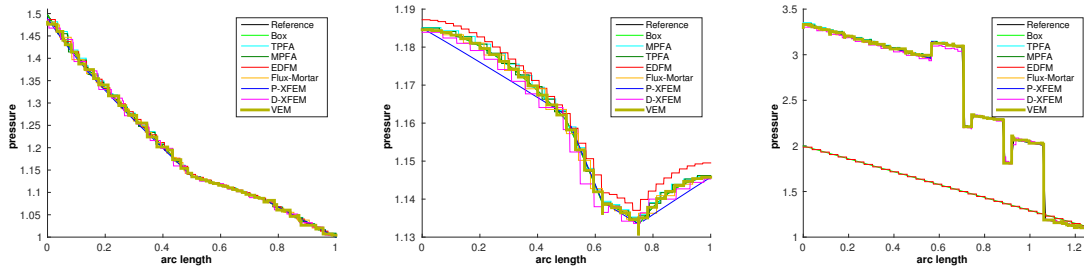


Figure 6: Benchmark 1 with conductive fractures. On the left: pressure along horizontal line at $y = 0.7$ with permeable fracture. On the centre: pressure along vertical fracture at $x = 0.5$ with permeable fractures. On the right: pressure along the line $(0.0,0.1) - (0.9,1.0)$ with blocking fractures.

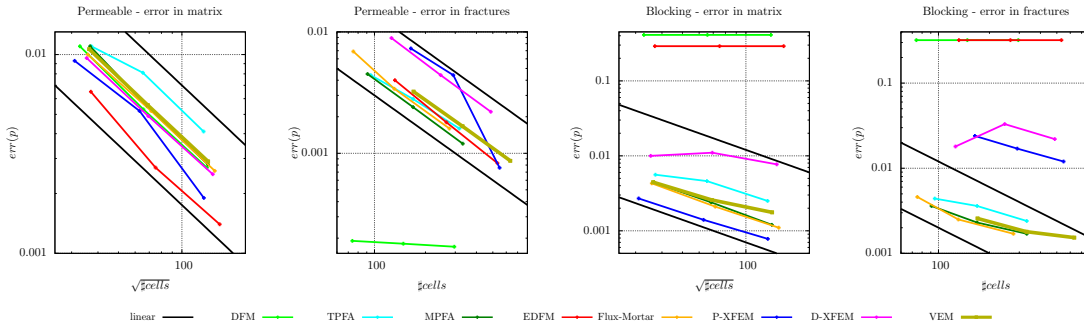


Figure 7: Benchmark 1, error evolution for the matrix and the fractures with conductive and blocking fractures.

and blocking fractures the error decay. The errors are comparable with others methods able to represent permeable and blocking fractures. In the latter case we notice a stagnancy of the fracture error bounding the order of converge, this phenomena is common also for other methods presented in the benchmark study [22].

5.1.2 Benchmark 4: a Realistic Case

We consider now a complex system of 64 fractures from a real outcrop. We consider constant rock permeability equal to 10^{-14}m^2 , uniform fracture permeability 10^{-8}m^2 , and fracture aperture 10^{-2}m . We impose a pressure gradient at the boundary from the left (1013250 Pa) to the right (0 Pa). Also in this case, a triangular grid is coarsened to reduce the grid complexity. The reference grid is composed by 12472 2d cells, 1317 1d cells, and 85 0d cells. The coarse algorithm decreases the 2d cells down to 4703. The total number of degrees of freedom is 19075 for the coarse grid.

The computed solution is represented in Figure 9 on the left, which matches the solution of the others method considered in [22]. Because of the complexity of the network, conforming and non-matching methods may pose a constraint to the grid generation in particular for close fractures. However, the method presented allows general grid cells lighten the computational cost for the simulation. We refer to Figure 8, which represents almost intersecting fractures.

As shown in Figure 8, some of the grid cells are non star-shaped or even contains cuts. For a more detailed discussion refer to [25]. Finally, to validate in more detail the computed solution we present two plots over line and compare them with the solutions obtained in the benchmark study, see Figure 9. The curves for the current method are in good agreement with the others. Small oscillations are related to mesh effects.

5.2 Passive scalar transport

In this part we consider both mixed-dimensional models (1) and (2) to simulate a passive scalar transport. We consider the geometry presented in Section 5.1.2 and compare the solution obtained with both grids in Figure 8 for permeable and blocking fractures. For the reference grid the total number of degrees of freedom is 35578. The aim of this test is to validate the quality of the Darcy velocity on the passive scalar in presence of the grid coarsening. In the following fracture aperture is constant and equal to 10^{-2}m , a pressure gradient from the right to left boundary of the domain of $3 \cdot 10^7\text{Pa}$, a final simulation time of 40 years.

5.2.1 Permeable fractures

We consider high permeable fractures with tangential permeability of $5 \cdot 10^{-6}\text{m}^2$ and normal permeability of $2.5 \cdot 10^{-9}\text{m}^2$. Matrix permeability is set to $2.5 \cdot 10^{-11}\text{m}^2$. Figure 10 compares the solutions obtained on the reference triangular grid and on the coarse grid. Moreover Figure 11 on the left presents a comparison of the passive scalar production. We notice the good agreement in both the pressure and concentration fields as well as in the production. We can conclude that in this case the grid coarsening is not affecting the quality of the computed solutions.

Finally in Figure 11 on the right the temporal error decay is reported. The spatial discretization is fixed and we consider a sequence of simulation with (10, 20, 40, 80, 160, 320, 640, 1280, 2560, 5120) time steps each. The error is computed as the L^2 difference from a reference solution obtained with 10^5 time steps after 10 years. A unitary error decay is achieved, coherent with the numerical scheme considered.

5.2.2 Blocking fractures

We consider low permeable fractures with tangential and normal permeability of $7.5 \cdot 10^{-16}\text{m}^2$. Matrix permeability is set to $7.5 \cdot 10^{-11}\text{m}^2$. Figure 12 compares the solutions obtained on the reference triangular grid and on the coarse grid. In this case we notice a pick of velocity in the reference case due to small elements close to almost intersecting fractures. This may affect an explicit in time solver. Figure 13 on the left presents a comparison of the passive scalar production. We notice the good agreement in both the pressure and concentration

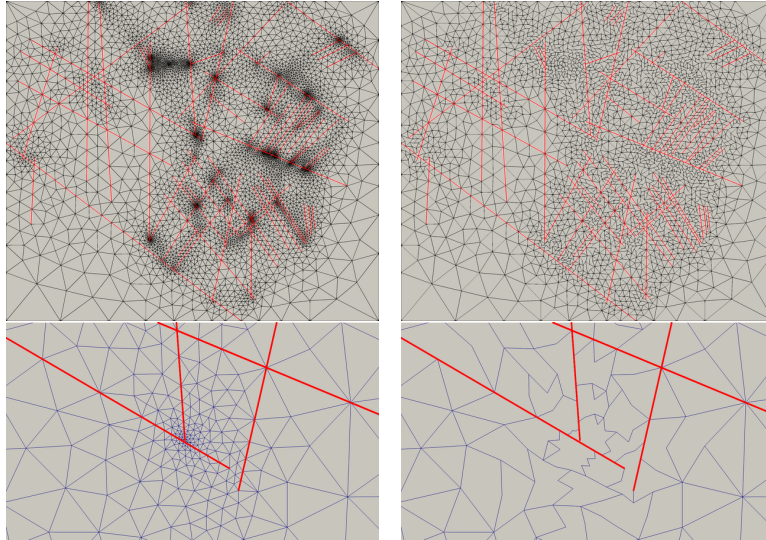


Figure 8: Benchmark 4. On the top: original grid composed by 12302 2d-cells and 35153 VEM *dof* and coarsened grid composed by 4599 2d-cells and 18803 VEM *dof*. On the bottom: a zoom on almost intersecting fractures for the original and coarsened grids, respectively. The zoom is referred to the small rectangle at position, approximately, (360, 350).

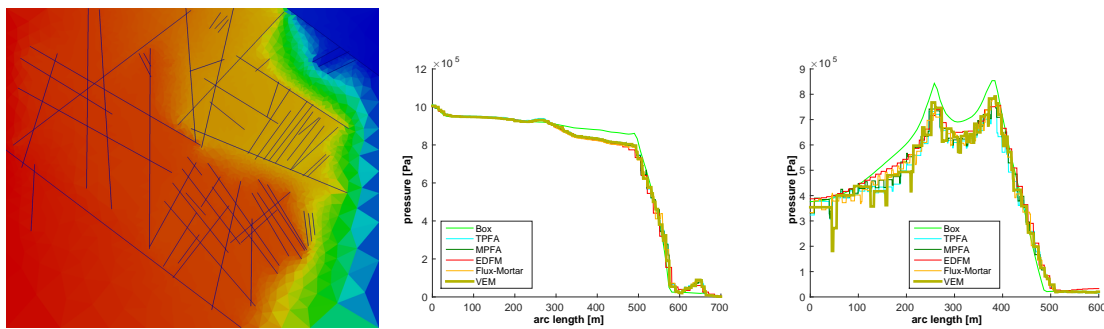


Figure 9: Benchmark 4. On the left: pressure solution computed with VEM. The pressure ranges in $[0, 1013250]$ Pa. On the centre: pressure along horizontal line at $y = 500\text{m}$. On the right: pressure along vertical line at $x = 625\text{m}$.

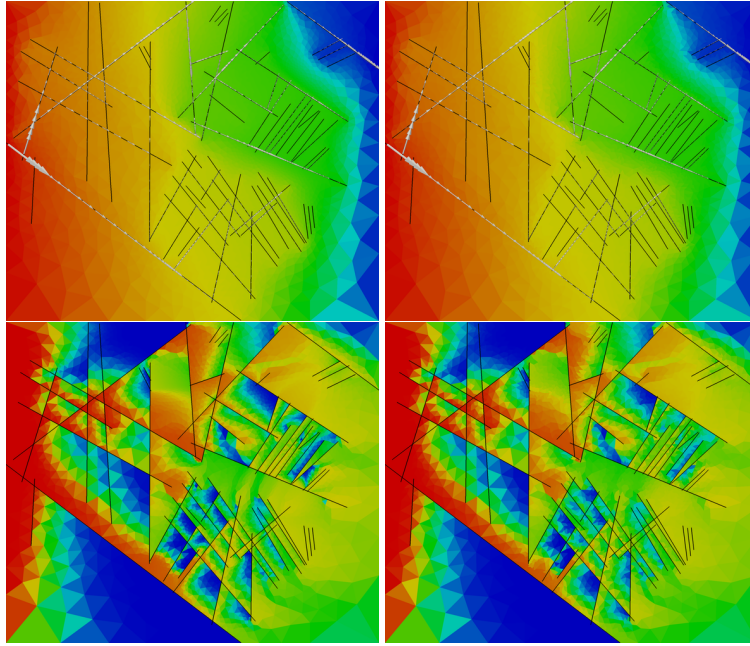


Figure 10: Permeable fractures. On the top: reference and coarse solutions for pressure and velocity, as arrows. On the bottom: reference and coarse solutions for concentration of the passive scalar.

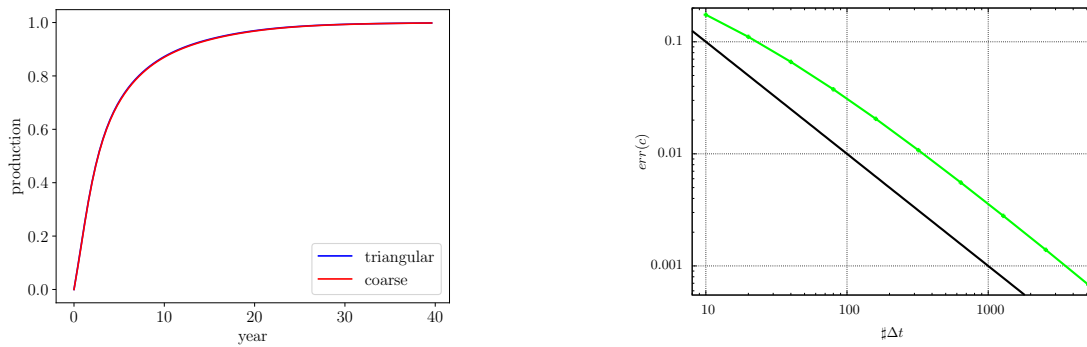


Figure 11: Permeable fractures. On the left: comparison of passive scalar production at the outflow between the reference triangular grid and the coarse grid. On the right: temporal error decay with reference $\mathcal{O}(\Delta t)$ in black.

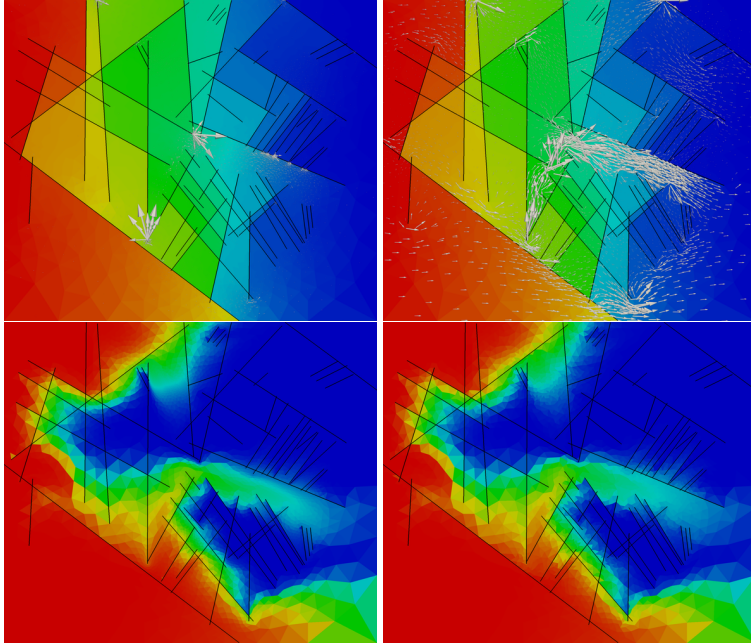


Figure 12: Blocking fractures. On the top: reference and coarse solutions for pressure and velocity, as arrows. On the bottom: reference and coarse solutions for concentration of the passive scalar.

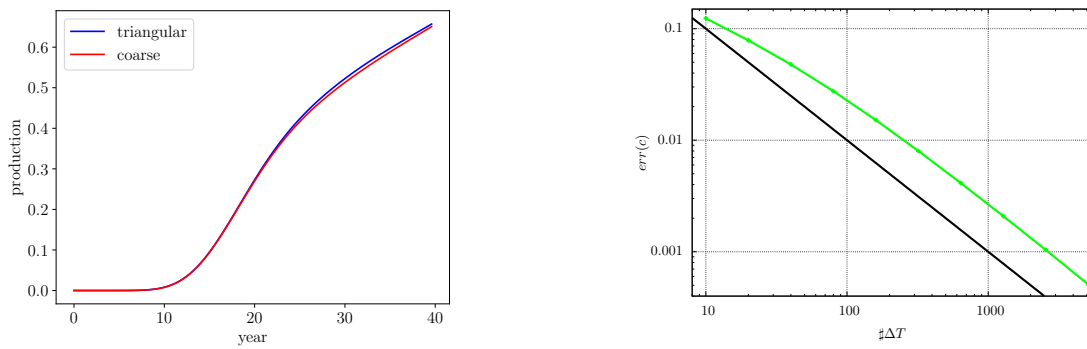


Figure 13: Blocking fractures. On the left: comparison of passive scalar production at the outflow between the reference triangular grid and the coarse grid. On the right: temporal error decay with reference $\mathcal{O}(\Delta t)$ in black.

fields as well as in the production. We can conclude that also in this case the grid coarsening is not affecting the quality of the computed solutions.

Again, the temporal error decay is reported, see Figure 13, right. The spatial discretization is fixed and we require (10, 20, 40, 80, 160, 320, 640, 1280, 2560, 5120) time steps, respectively. A unitary error decay is achieved, consistent with the numerical scheme considered.

5.3 Passive scalar transport on a realistic 3d-network

In this example we consider a realistic geometry for a geothermal system. We study a partial reconstruction of fractures from test site at Soultz-sous-Forêts in France, for more details see [43]. The network is composed by 20 fractures represented as polygons with 10 edges each. The fracture intersections result in 33 1d objects and 4 0d objects. In this case the full model is needed to accurately simulate the fluid flow and transport on the domain. The fracture geometry is represented in Figure 14. We assume rock matrix permeability as $7.5 \cdot 10^{-10} \text{m}^2$ and fracture permeability, in both the normal and tangential direction, equal to $5 \cdot 10^{-5} \text{m}^2$. The fracture aperture is $\epsilon^2 = 10^{-2} \text{m}$ and, for the lower dimensional objects, we consider their “aperture” as the square and the cube of the fracture aperture, respectively for the 1d and 0d objects. We impose a pressure from the top to bottom of the domain and no flux boundary conditions on the other sides. The reference grid is composed by 44331 tetrahedra, 6197 triangles for the 2d grids, 151 segments for the 1d grids, and 4 point-cells for the 0d grids. After the coarsening algorithm the resulting grid is composed by 16108 polyhedra, and for the lower dimensional objects the grids are untouched. See Figure 16 on the right for an example of coarse cells. The transport simulation runs for 40 years and, for the implicit Euler scheme, we consider 100 time steps.

The objective is to study the robustness of the virtual elements associated with the coarsening strategy and detect if the coarse model gives accurately enough results. The pressure solution and the concentration of the scalar passive are depicted in Figures 14 and 15, respectively, for both the reference and coarse case. Both the pressure and concentration profiles for the two grids are in good agreement. To analyse the macroscopic behaviour of the resulting solution a production curve comparison is reported in Figure 16, showing a small discrepancy from the reference and the coarse production.

We can conclude that also in this case the adopted strategy is effective and can be applied to complex system of fractures, ensuring a good compromise between high accuracy and computational effort.

6 Conclusions

In the paper we presented two classes of mixed-dimensional problems able to describe a single-phase flow and a transport of a scalar passive in fractured porous media. The latter is transported by the Darcy velocity computed by the former model. The considered mixed-dimensional Darcy problem is able to represent channel and barrier behaviours of fractures as well as their intersections. The models represent thus a comprehensive description of this phenomena, which are key ingredients for the description of several energy application problems. The numerical scheme considered for the discretization of the Darcy equation are able to handle, supported by theoretical findings, grid cells of arbitrary geometry becoming a strong advantage when dealing with high and complex fractured porous media. Numerical results have shown the capability to apply this strategy obtaining accurate outcomes with a reasonable computational cost. The transport model can be viewed as a first attempt to introduce a full model for the description of heat exchange in a porous media, which will be a part of future investigations.

Acknowledgment

We acknowledge financial support for the ANIGMA project from the Research Council of Norway (project no. 244129/E20) through the ENERGIX program. The authors warmly thank the others components of the ANIGMA project team: Eivind Bastesen, Inga Berre,

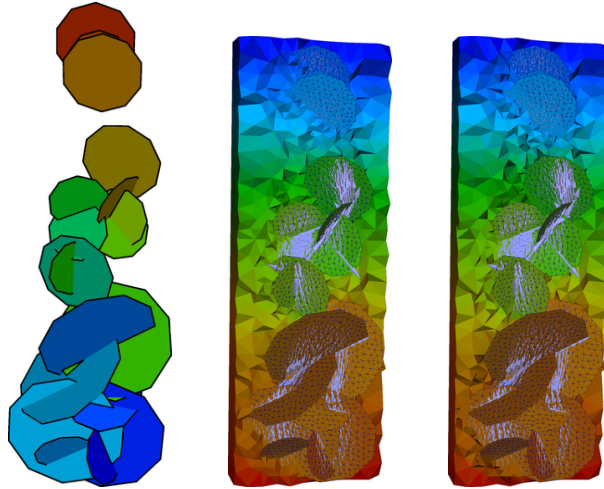


Figure 14: On the left representation of the 20 fractures coloured by their identification number. Pressure and velocity for both the reference and coarse grids. The pressure is scaled between 0 and $4.8 \cdot 10^7$.

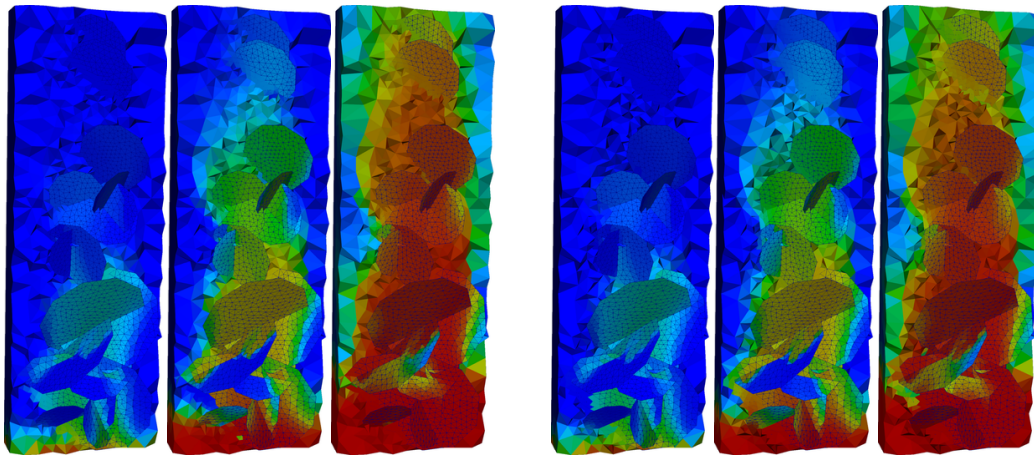


Figure 15: On the left three time steps on the reference grid for the concentration. On the right, at the same steps, the concentration computed on the coarse grid.

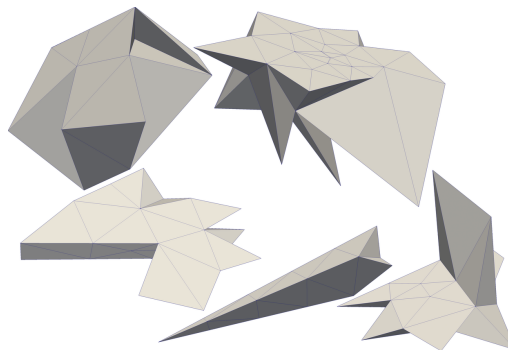
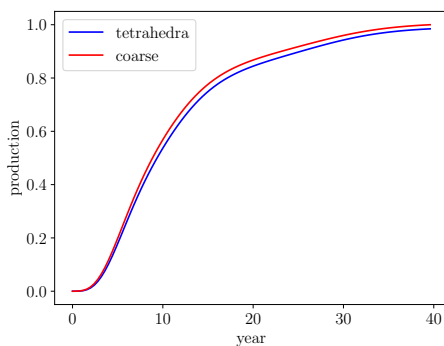


Figure 16: On the left the production comparison between the reference and the coarse solution. On the right an example of five coarse cells.

Simon John Buckley, Casey Nixon, David Peacock, Atle Rotevatn, Pål Næverlid Sævik, Luisa F. Zuluaga.

The authors wish to thank also: Runar Berge, Wietse Boon, Ivar Stefansson, Eren Uçar.

References

- [1] Clarisse Alboin, Jérôme Jaffré, Jean E. Roberts, Xuewen Wang, and Christophe Serres. *Domain decomposition for some transmission problems in flow in porous media*, volume 552 of *Lecture Notes in Phys.*, pages 22–34. Springer, Berlin, 2000.
- [2] Laila Amir, Michel Kern, Vincent Martin, and Jean E. Roberts. Décomposition de domaine et préconditionnement pour un modèle 3D en milieu poreux fracturé. In *Proceeding of JANO 8, 8th conference on Numerical Analysis and Optimization*, December 2005. 2005.
- [3] Philippe Angot. A model of fracture for elliptic problems with flux and solution jumps. *Comptes Rendus Mathématique*, 337(6):425–430, 2003.
- [4] Philippe Angot, Franck Boyer, and Florence Hubert. Asymptotic and numerical modelling of flows in fractured porous media. *M2AN Math. Model. Numer. Anal.*, 43(2):239–275, 2009.
- [5] Paola Francesca Antonietti, Luca Formaggia, Anna Scotti, Marco Verani, and Nicola Verzotti. Mimetic finite difference approximation of flows in fractured porous media. *ESAIM: M2AN*, 50(3):809–832, 2016.
- [6] Lourenço Beirão da Veiga, Franco Brezzi, Luisa Donatella Marini, and Alessandro Russo. H(div) and H(curl)-conforming VEM. *ArXiv e-prints*, July 2014.
- [7] Lourenço Beirão da Veiga, Franco Brezzi, Luisa Donatella Marini, and Alessandro Russo. The hitchhiker’s guide to the virtual element method. *Mathematical Models and Methods in Applied Sciences*, 24(08):1541–1573, 2014.
- [8] Lourenço Beirão da Veiga, Franco Brezzi, Luisa Donatella Marini, and Alessandro Russo. Mixed virtual element methods for general second order elliptic problems on polygonal meshes. *ESAIM: M2AN*, 50(3):727–747, 2016.
- [9] Matías Fernando Benedetto, Stefano Berrone, Andrea Borio, Sandra Pieraccini, and Stefano Scialò. A hybrid mortar virtual element method for discrete fracture network simulations. *Journal of Computational Physics*, 306:148 – 166, 2016.
- [10] Matías Fernando Benedetto, Stefano Berrone, Sandra Pieraccini, and Stefano Scialò. The virtual element method for discrete fracture network simulations. *Computer Methods in Applied Mechanics and Engineering*, 280(0):135–156, 2014.
- [11] Stefano Berrone, Sandra Pieraccini, and Stefano Scialò. A PDE-constrained optimization formulation for discrete fracture network flows. *SIAM Journal on Scientific Computing*, 35(2), 2013.
- [12] Stefano Berrone, Sandra Pieraccini, and Stefano Scialò. On simulations of discrete fracture network flows with an optimization-based extended finite element method. *SIAM Journal on Scientific Computing*, 35(2):908–935, 2013.
- [13] Wietse M. Boon, Jan M. Nordbotten, and Jon E. Vatne. Mixed-dimensional elliptic partial differential equations. Technical report, arXiv:1710.00556 [math.AP], 2017.
- [14] Wietse M. Boon, Jan Martin Nordbotten, and Ivan Yotov. Robust discretization of flow in fractured porous media. Technical report, arXiv:1601.06977v2 [math.NA], 2017.
- [15] Konstantin Brenner, Julian Hennicker, Roland Masson, and Pierre Samier. Gradient discretization of hybrid-dimensional Darcy flow in fractured porous media with discontinuous pressures at matrix-fracture interfaces. *IMA Journal of Numerical Analysis*, September 2016.
- [16] Kostantin Brenner, Mayya Groza, C. Guichard, and Roland Masson. Vertex approximate gradient scheme for hybrid dimensional two-phase darcy flows in fractured porous media. *ESAIM: Mathematical Modelling and Numerical Analysis*, 49(2):303–330, 2015.

- [17] Franco Brezzi, Richard S. Falk, and Donatella Luisa Marini. Basic principles of mixed virtual element methods. *ESAIM: M2AN*, 48(4):1227–1240, 2014.
- [18] Florent A Chave, Daniele Di Pietro, and Luca Formaggia. A Hybrid High-Order method for Darcy flows in fractured porous media. Technical report, HAL archives, 2017.
- [19] Carlo D’Angelo and Anna Scotti. A mixed finite element method for Darcy flow in fractured porous media with non-matching grids. *Mathematical Modelling and Numerical Analysis*, 46(02):465–489, 2012.
- [20] Marco Del Pra, Alessio Fumagalli, and Anna Scotti. Well posedness of fully coupled fracture/bulk darcy flow with xfem. *SIAM Journal on Numerical Analysis*, 55(2):785–811, 2017.
- [21] Isabelle Faille, Alessio Fumagalli, Jérôme Jaffré, and Jean Elisabeth Roberts. Model reduction and discretization using hybrid finite volumes of flow in porous media containing faults. *Computational Geosciences*, 20(2):317–339, 2016.
- [22] Bernd Flemisch, Inga Berre, Wietse Boon, Alessio Fumagalli, Nicolas Schwenck, Anna Scotti, Ivar Stefansson, and Alexandru Tatomir. Benchmark of single-phase flow in fractured porous media with non-conforming discretization methods. Accepted in: *Advances in Water Resources*, available at arXiv:1701.01496 [math.NA], 2017.
- [23] Luca Formaggia, Alessio Fumagalli, Anna Scotti, and Paolo Ruffo. A reduced model for Darcy’s problem in networks of fractures. *ESAIM: Mathematical Modelling and Numerical Analysis*, 48:1089–1116, 7 2014.
- [24] Najla Frih, Vincent Martin, Jean Elisabeth Roberts, and Ai Saâda. Modeling fractures as interfaces with nonmatching grids. *Computational Geosciences*, 16(4):1043–1060, 2012.
- [25] Alessio Fumagalli. Dual virtual element method in presence of an inclusion. Technical report, arXiv:1709.03519 [math.NA], 2017.
- [26] Alessio Fumagalli and Eirik Keilegavlen. Dual virtual element method for discrete fractures networks. Accepted in: *SIAM Journal on Scientific Computing (SISC)*, available at: arXiv:1610.02905 [math.NA], 2017.
- [27] Alessio Fumagalli, Luca Pasquale, Stefano Zonca, and Stefano Micheletti. An upscaling procedure for fractured reservoirs with embedded grids. *Water Resources Research*, 52(8):6506–6525, 2016.
- [28] Alessio Fumagalli and Anna Scotti. A numerical method for two-phase flow in fractured porous media with non-matching grids. *Advances in Water Resources*, 62, Part C(0):454–464, 2013. *Computational Methods in Geologic CO2 Sequestration*.
- [29] Alessio Fumagalli and Anna Scotti. A Reduced Model for Flow and Transport in Fractured Porous Media with Non-matching Grids. In Andrea Cangiani, Ruslan L. Davidchack, Emmanuil Georgoulis, Alexander N. Gorban, Jeremy Levesley, and Michael V. Tretyakov, editors, *Numerical Mathematics and Advanced Applications 2011*, pages 499–507. Springer Berlin Heidelberg, 2013.
- [30] Alessio Fumagalli and Anna Scotti. An Efficient XFEM Approximation of Darcy Flows in Arbitrarily Fractured Porous Media. *Oil and Gas Sciences and Technologies - Revue d’IFP Energies Nouvelles*, 69(4):555–564, April 2014.
- [31] Alessio Fumagalli, Stefano Zonca, and Luca Formaggia. Advances in computation of local problems for flow-based upscaling in fractured reservoirs. *Mathematics and Computers in Simulation*, 137:299 – 324, July 2017.
- [32] Sebastian Geiger, Marco Dentz, and Insa Neuweiler. A novel multi-rate dual-porosity model for improved simulation of fractured and multiporosity reservoirs. *SPE Reservoir Characterisation and Simulation Conference and Exhibition*, pages –, 2011.
- [33] Christophe Geuzaine and Jean-François Remacle. Gmsh: A 3-d finite element mesh generator with built-in pre- and post-processing facilities. *International Journal for Numerical Methods in Engineering*, 79(11):1309–1331, 2009.
- [34] Mohammad Karimi-Fard and Luis J. Durlofsky. A general gridding, discretization, and coarsening methodology for modeling flow in porous formations with discrete geological features. *Advances in Water Resources*, 96:354–372, oct 2016.

- [35] Mohammad Karimi-Fard and Abbas Firoozabadi. Numerical simulation of water injection in fractured media using the discrete-fracture model and the galerkin method. *SPE Reservoir Evaluation & Engineering*, 6(02):117–126, 2003.
- [36] Mohammad Karimi-Fard, Bin Gong, and Luis J. Durlofsky. Generation of coarse-scale continuum flow models from detailed fracture characterizations. *Water Resources Research*, 42(10), 2006.
- [37] Peter Knabner and Jean Elisabeth Roberts. Mathematical analysis of a discrete fracture model coupling darcy flow in the matrix with darcy-forchheimer flow in the fracture. *ESAIM: Mathematical Modelling and Numerical Analysis*, 48:1451–1472, 9 2014.
- [38] Liyong Li and Seong H. Lee. Efficient field-scale simulation of black oil in a naturally fractured reservoir through discrete fracture networks and homogenized media. *SPE Reservoir Evaluation & Engineering*, 11:750–758, 2008.
- [39] Vincent Martin, Jérôme Jaffré, and Jean Elisabeth Roberts. Modeling Fractures and Barriers as Interfaces for Flow in Porous Media. *SIAM J. Sci. Comput.*, 26(5):1667–1691, 2005.
- [40] Valeri V. Mourzenko, Jean-François Thovert, and Pierre M. Adler. Permeability of isotropic and anisotropic fracture networks, from the percolation threshold to very large densities. *Phys. Rev. E*, 84:036307, Sep 2011.
- [41] Pål Næverlid Sævik, Inga Berre, Morten Jakobsen, and Martha Lien. A 3d computational study of effective medium methods applied to fractured media. *Transport in Porous Media*, 100(1):115–142, Oct 2013.
- [42] Pål Næverlid Sævik, Morten Jakobsen, Martha Lien, and Inga Berre. Anisotropic effective conductivity in fractured rocks by explicit effective medium methods. *Geophysical Prospecting*, 62(6):1297–1314, 2014.
- [43] Judith Sausse, Chrystel Dezayes, Louis Dorbath, Albert Genter, and Joachim Place. 3d model of fracture zones at soultz-sous-forêts based on geological data, image logs, induced microseismicity and vertical seismic profiles. *Comptes Rendus Geoscience*, 342(7):531–545, 2010.
- [44] Nicolas Schwenck, Bernd Flemisch, Rainer Helmig, and BarbaraI. Wohlmuth. Dimensionally reduced flow models in fractured porous media: crossings and boundaries. *Computational Geosciences*, 19(6):1219–1230, 2015.
- [45] Anna Scotti, Luca Formaggia, and Federica Sottocasa. Analysis of a mimetic finite difference approximation of flows in fractured porous media. *ESAIM: M2AN*, 2017.
- [46] Matei Tene, Mohammed Saad Al Kobaisi, and Hadi Hajibeygi. Multiscale projection-based embedded discrete fracture modeling approach (f-ams-pedfm). In *ECMOR XIV-15th European Conference on the Mathematics of Oil Recovery*. EAGE, 2016.
- [47] Xavier Tunc, Isabelle Faille, Thierry Gallouët, Marie Christine Cacas, and Pascal Havé. A model for conductive faults with non-matching grids. *Computational Geosciences*, 16:277–296, 2012.